Detection of Substructure in the Gravitationally Lensed Quasar MG0414+0534 using Mid-Infrared and Radio VLBI Observations

Chelsea L. MacLeod[1], Ramsey Jones[2], Eric Agol[2], and Christopher S. Kochanek[3]

Received _____; accepted _____

[1]Physics Department, United States Naval Academy, Annapolis, MD 21403; macleod@usna.edu

[2]Astronomy Department, University of Washington, Seattle, WA 98195

[3]Department of Astronomy and the Center for Cosmology and Astroparticle Physics, The Ohio State University, Columbus, OH 43210

ABSTRACT

We present 11.2 μm observations of the gravitationally lensed, radio-loud $z_s = 2.64$ quasar MG0414+0534, obtained using the Michelle camera on Gemini North. We find a flux ratio anomaly of A2/A1 = 0.93±0.02 for the quasar images A1 and A2. When combined with the 11.7 μm measurements from Minezaki et al. (2009), the A2/A1 flux ratio is nearly 5σ from the expected ratio for a model based on the two visible lens galaxies. The mid-IR flux ratio anomaly can be explained by a satellite (substructure), 0.″3 Northeast of image A2, as can the detailed VLBI structures of the jet produced by the quasar. When we combine the mid-IR flux ratios with high-resolution VLBI measurements, we find a best-fit mass of $10^{7.3\pm0.2}$ $M_\odot$ inside the Einstein radius for a satellite substructure modeled as a singular isothermal sphere at the redshift of the main lens ($z_l = 0.96$). We are unable to set an interesting limit on the mass to light ratio due to its proximity to the quasar image A2. While the observations used here were technically difficult, surveys of flux anomalies in gravitational lenses with the *James Webb Space Telescope* will be simple, fast, and should well constrain the abundance of substructure in dark matter haloes.

1. Introduction

The missing satellite problem, where cosmological simulations of cold dark matter (CDM) predict a significantly larger fraction of lower mass satellites around galaxies than is detected, represents a major puzzle in the study of structure formation (Klypin et al. 1999; Moore et al. 1999). In the case of the Milky Way, the Sloan Digital Sky Survey has steadily found additional, faint satellites, but the total numbers are still far lower than the expected abundances of subhaloes (e.g., Willman et al. 2005; Belokurov et al. 2007). The

simplest solution in the context of CDM models is to suppress star formation in low-mass satellites, probably through heating and baryonic mass loss as the universe re-ionizes to leave a population of dark satellites (e.g., Klypin et al. 1999; Bullock et al. 2000) with assistance from the relative streaming of baryons and dark matter after recombination (Tseliakhovich & Hirata 2010). Locally there is some hope of finding these dark satellites through γ-rays emitted by dark matter annihilation, but the likelihood of detection depends heavily on the properties of dark matter (e.g., Strigari et al. 2008).

Gravitational lensing offers an alternate method to detect subhaloes. In some strong lenses (e.g. MG0414+0534, Ros et al. 2000; MG2016+112, Kochanek 2006; HE0435–1223, Kochanek et al. 2006, Fadely & Keeton 2012; B1938+666, Vegetti et al. 2012), satellite galaxies of the primary lens can be detected astrometrically through their effects on the image positions. Potentially, the most massive satellites can also be detected through their effects on time delay ratios (Keeton & Moustakas 2009). But as emphasized by Mao & Schneider (1998) and Metcalf & Zhao (2002), image fluxes are sensitive to perturbations even from very low-mass satellites ($\lesssim 10^6 M_\odot$). Moreover, we observe many lenses with "flux ratio anomalies" where the relative image brightnesses cannot be explained by simple, central lens galaxies (see Evans & Witt 2003; Kochanek & Dalal 2004; Congdon & Keeton 2005; Yoo et al. 2006a,b; Kratzer et al. 2011). While current results are consistent with the expectations of CDM (Dalal & Kochanek 2002; Vegetti et al. 2012), there are still too few lenses to precisely test the CDM model using flux ratio anomalies. For this technique, the challenge is that image fluxes can also be affected by extinction and microlensing in the primary lens at the most easily observed wavelengths, although the wavelength dependencies of these three effects can help to disentangle them from each other (e.g., Agol et al. 2009; Muñoz et al. 2011). The millilensing signal by substructures is best isolated at radio or rest-frame mid-infrared (mid-IR, $\sim$4–100 μm) wavelengths, where both extinction and microlensing effects from the lens galaxy are negligible (stars

can only magnify sources smaller than ∼0.1 pc). The mid-IR images are also unaffected by interstellar scattering, or scintillation, which can further perturb the radio images, although few lenses show the strong radio wavelength-dependent signatures expected from these effects (Kochanek & Dalal 2004). The biggest problem for using radio wavelengths is simply that most quasars are radio-quiet, leaving only a handful of objects to be studied. While mid-IR observations are challenging, they are ideal for searching for substructures in lens galaxies.

Here we present mid-IR observations of the quadruply lensed, radio-loud $z_s = 2.64$ quasar MG0414+0534, obtained using the Michelle camera on Gemini North. This system is known to be affected by extinction and microlensing in the optical and near-IR (Hewitt et al. 1992; Lawrence et al. 1995; Falco et al. 1997; Bate et al. 2008, 2011; Pooley et al. 2012), but the flux ratio anomaly persists into the mid-IR and radio. Our new measurements have slightly higher precision than those by Minezaki et al. (2009) and we then consider more detailed models. This work is an extension of the study in MacLeod et al. (2009), where a companion lens galaxy was detected through the mid-IR flux ratios of the four-image lens H1413+117. Here, we show that the flux ratio anomaly in MG0414+0534 indicates the presence of low-mass substructure in the lens based on models of the individual or combined radio and mid-IR observations of this lens. Our data are described in Section 2, our lens models are presented in Section 3, and our conclusions are in Section 4.

2. Flux measurements and errors

We observed MG0414+0534 with the Michelle camera (Roche 2004) on Gemini North at 11.2 μm (F112B21 filter) on 2 Jan 2006. The observing time was 1 hour, of which 940.8 seconds were spent on source. The data were processed with the standard Gemini pipeline *mireduce*. Our analysis starts with the coadded chop and nod subtracted image. These

initial images have 16 vertical stripes due to the 16 readout channels. We corrected for the stripes by subtracting the median of each stripe after masking the region containing the quasar images. This procedure also removes any residual sky flux. Figure 1 shows the resulting image.

We fit the four lensed images using a 2-D Gaussian to model the PSF, fixing the relative image positions to those measured from the *Hubble Space Telescope* (*HST*) images[1] (Falco et al. 1997). Since the sky is so much brighter than the quasar images, we use the standard deviation of the background pixels as an estimate of the errors in the flux of each pixel. The model has nine free parameters: the fluxes of the four images (4), the position of image B (2), the standard deviation of the Gaussian PSF along the two principal directions (2), and the angle of the major axis. We found the best-fit model using non-linear Levenberg-Marquardt optimization. We used a Markov chain Monte Carlo (MCMC) with 10^4 steps to compute the parameter uncertainties, and ran multiple chains to check the convergence of the best-fit parameters and their uncertainties. We also estimated the errors by simply computing the goodness of fit as a function of the flux of each image, marginalizing over all other variables.

Figure 1 shows the best-fit model and its residuals, and Figure 2 shows the MCMC and $\Delta\chi^2$ estimate for the fluxes (in arbitrary units) and their uncertainties. In order to include any covariances between the image fluxes, we use the actual distribution of flux ratios from the MCMC approach to estimate the flux ratio uncertainties. We calibrated the flux measurements using observations of the standard star Rho Orionis (HR 1698) and the Cohen et al. (1999) flux calibration at 11.2 μm (the interpolated flux is $\simeq$ 6.43 Jy). We obtained a total flux of 33.4 ± 1.3(statistical) ± 3.2(systematic) mJy at 11.2 μm from aperture photometry, which is lower than the value of 39.2 ± 1.4 mJy in Minezaki et al.

[1]http://www.cfa.harvard.edu/castles/

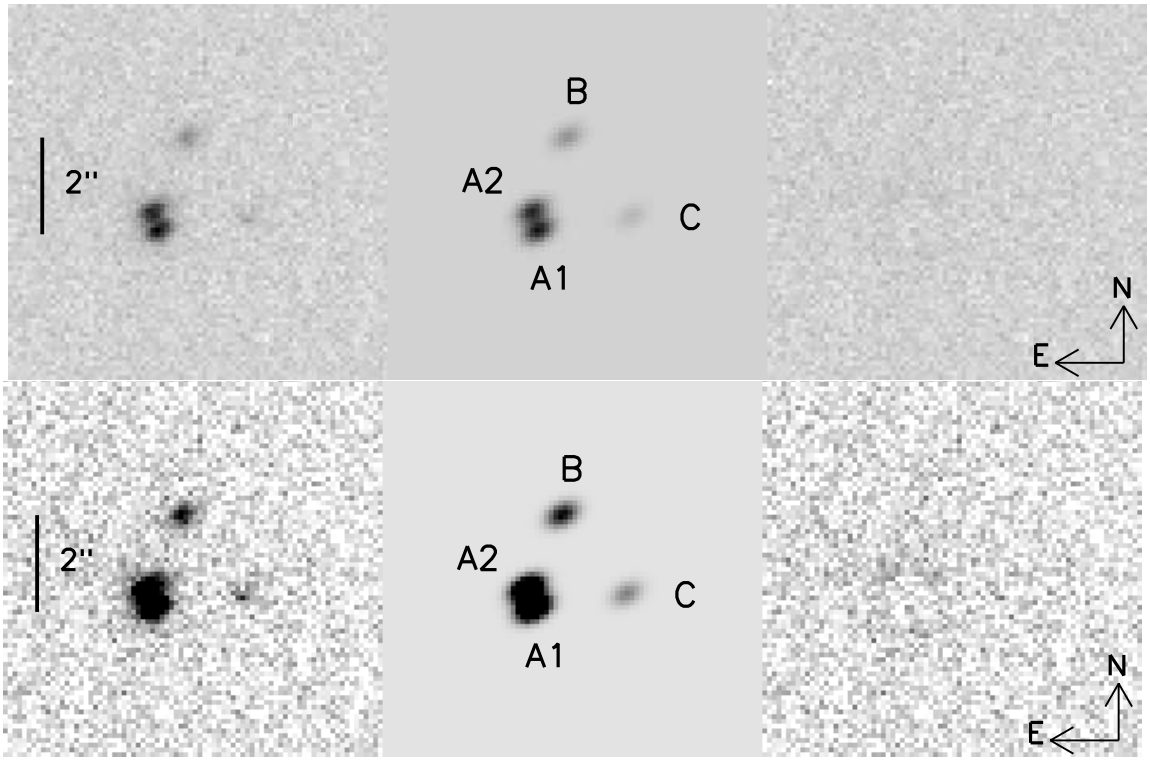

Fig. 1.— The left, middle, and right panels show the 11.2 μm data, the best-fit model based on 2-D Gaussians, and the model residuals, respectively, for MG0414+0534. In the bottom panels, the images have been scaled to increase the visibility of B and C.

(2009). This discrepancy may be due to the fact that our filter has a shorter central wavelength and that the SED is rising towards longer wavelengths. The resulting mid-IR flux ratios are listed in Table 1 along with the mid-IR results from Minezaki et al. (2009), and the combined results. The results agree given their mutual uncertainties and show that the anomaly, while not as strong as in the near-IR (Bate et al. 2008), persists into the mid-IR. This wavelength behavior is a first indication that the anomalous flux ratio in the near-IR is not produced solely by microlensing, as assumed in Bate et al. (2008), but also by substructure in the lens.

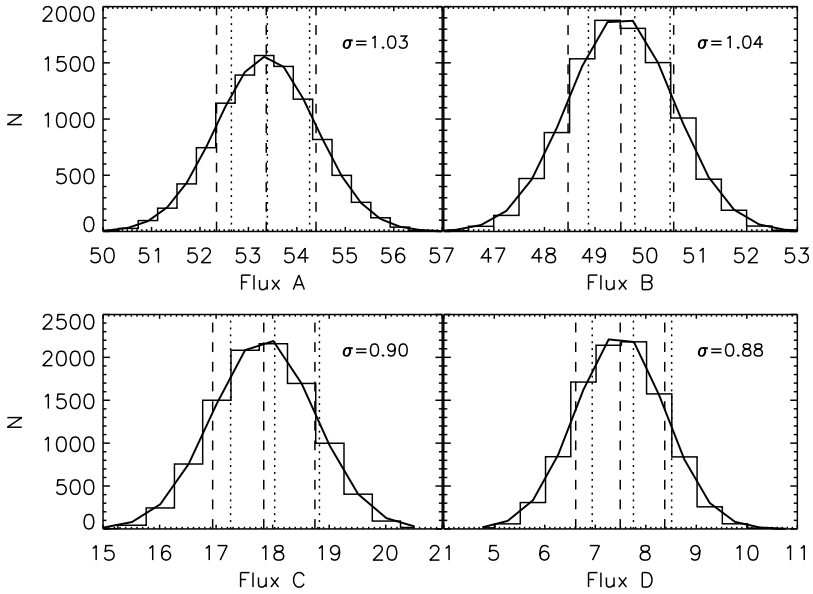

Fig. 2.— MCMC probability distributions for the MG0414+0534 image fluxes (in arbitrary units). The vertical dashed lines show the mean and 1σ error bars determined from the best-fit Gaussian curve. These are compared to the best-fit flux value and 68% confidence limits (or parameter values at which $\Delta\chi^2 = 1$ from the minimum χ^2) that result from the χ^2 minimization technique (see text), which are shown by vertical dotted lines. The Gaussian widths (σ) are listed in the top right corners. For the uncertainties reported in Table 1, we instead use the dispersion of flux *ratios* from the MCMC.

Table 1. Relative Mid-IR Fluxes for the Images of MG0414+0534

Images	Flux Ratio		
	This work	Minezaki et al. (2009)	Combined
A2/A1	0.926 ± 0.025	0.90 ± 0.04	0.919 ± 0.021
B/A1	0.338 ± 0.017	0.36 ± 0.02	0.347 ± 0.013
C/A1	0.145 ± 0.016	0.12 ± 0.03	0.139 ± 0.014

3. Models

In a multiple-image strong gravitational lens, a close pair of bright images such as A1 and A2 results if the quasar is near a fold caustic created by the main lens galaxy. Their flux ratio is expected to be unity for a smooth lens model (e.g., Keeton et al. 2005), whereas we measure a flux ratio of A2/A1 $= 0.93 \pm 0.02$ for MG0414+0534. Since we are insensitive to extinction or microlensing effects created by the lens galaxy in the mid-IR, the anomalous ratio must be attributed to millilensing by substructure in the lens, as was also argued by Minezaki et al. (2009).

We model the system with LENSMODEL[2] (Keeton 2001), using the combined mid-IR flux ratios listed in Table 1 (last column) as constraints on our models. We use the measured *HST* WFPC/WFPC2 positions of the main, central lens galaxy, the secondary lens "X" (Schechter & Moore 1993; Ros et al. 2000), and the image positions from the CASTLES database (Falco et al. 1997). The component positions are listed in Table 2. The main lens galaxy (G1) is modeled as a singular isothermal ellipsoid (SIE) combined with an external shear, as this is the simplest plausible model for a lens. There is considerable evidence in favor of the isothermal profile, and the properties of 4-image systems other than time delays are very insensitive to the radial mass distribution (see Kochanek 2006; Koopmans et al. 2009). We include weak priors on the ellipticity of the main lens ($1 - b/a = 0 \pm 1$), and the external shear ($\gamma = 0.05 \pm 0.05$). The expectation value of 0 for the ellipticity is based on the relatively round isophotes derived from the *HST* photometry of the lens (Falco et al. 1997). For object X (hereafter "G2"), we tried two different models: a singular isothermal sphere (SIS) or a pseudo-Jaffe (pJaffe) profile with a scale length a' that is allowed to vary.

Using the mid-IR flux ratios as constraints, we obtain the best-fit two–galaxy models

[2]http://redfive.rutgers.edu/∼keeton/gravlens/

Table 2. MG0414+0534 Image and Lens Positions

MG0414 component	HST position (")	Rotated 0.1° (")	Error (")
A1	$(-0.600, -1.942)$	$(-0.596, -1.943)$	0.003
A2	$(-0.732, -1.549)$	$(-0.729, -1.550)$	0.003
B	$(0.000, 0.000)$	$(0.000, 0.000)$	0.003
C	$(1.342, -1.650)$	$(1.345, -1.648)$	0.003
G1	$(0.472, -1.277)$	$(0.474, -1.276)$	0.003
G2 (=X)	$(0.857, 0.180)$	$(0.857, 0.181)$	0.011

Note. — The positions are taken from the CASTLES database (Falco et al. 1997) and are relative to image B, where negative R.A. values are eastward of image B. We rotate the positions counter-clockwise by 0.1° when adding the radio constraints to our lens models.

described in Table 3. The models have 17 total constraints (the positions of 4 lensed images and both lens galaxies, the 3 flux ratios, plus the priors on the ellipticity e and shear γ) and 12 free parameters (the mass scale b_1, position, ellipticity e and position angle θ_e for G1, the amplitude γ and position angle θ_γ of the external shear, the mass scale b_2 and position for G2, and the source position), plus one more free parameter for the scale length a_2' when using a pseudo-Jaffe profile. In the Table, we describe our best two–galaxy models when using SIE+SIS or SIE+pJaffe profiles. We find a slightly better fit when using an SIS profile for G2, with $\chi^2 = 31.1$ for dof=5 degrees of freedom and a best-fit flux ratio $A2/A1 = 1.01$. The discrepancy between the observed and predicted mid-IR flux ratios in our two–galaxy models suggests the presence of substructure along the line of sight or associated with the main lens galaxy at nearly a 5σ level.

We modeled the substructure by adding a third lens galaxy (G3) with an SIS profile at various positions surrounding the lens and searched for a better fit to the observed flux ratios. Here, we adopt an SIS rather than a pseudo-Jaffe profile for G2 since the former yielded a better fit among the two–galaxy models. At each position in the grid, the mass scales b_1, b_2, and b_3 for galaxies G1, G2, and G3 were allowed to vary, as well as the ellipticity of G1 and the external shear, until a best-fit three–galaxy model was obtained. Here, dof=6, since we are holding the positions for G1 and G2 fixed for each model. Figure 3 (left panel) shows the resulting $\Delta\chi^2$ (relative to the two–galaxy model). It can be seen that the addition of substructure improves the two–galaxy model when placed Northeast or Northwest of image A2, although the range of positions that lead to a similar improvement is more limited Northwest of A2. We use this approximate location for G3 (Northeast of A2) as a starting point in our three–galaxy model and obtain the best-fit parameters in Table 3, where the coordinates of G3 are treated as free parameters. We find that an SIS with $b_3 \approx 0\farcs0028$ located at $(x_3, y_3) = (-0\farcs91, -1\farcs56)$ leads to the best improvement, with $\Delta\chi^2 = 25$ ($\chi^2/\mathrm{dof} = 3$). Assuming the measured redshift of

Table 3. MG0414+0534 Modeling Results

	G1+G2(pJaffe)	G1+G2	G1+G2+G3	G1+G2	G1+G2+G3
	(Mid-IR only)			**(Mid-IR + radio)**	
χ^2/dof	28.8/4	31.1/5	6.11/2	103/41	59.5/38
χ^2_{pos}	4.83	5.46	0.142	8.45	5.51
χ^2_{flux}	22.7	23.9	4.71	90.5	52.1
χ^2_{gal}	0.746	1.18	0.539	3.17	1.06
χ^2_{prior}	0.613	0.634	0.720	0.928	0.849
b_1	$1\farcs104$	$1\farcs068$	$1\farcs091$	$1\farcs083$	$1\farcs084$
e	0.298	0.302	0.224	0.242	0.238
θ_e (°E of N)	−88.5	−88.0	−85.4	−84.5	−83.9
γ	0.086	0.087	0.091	0.097	0.094
θ_γ (°E of N)	47.5	47.2	54.7	53.6	53.1
b_2	$0\farcs199$	$0\farcs193$	$0\farcs170$	$0\farcs185$	$0\farcs176$
a_2'	$2\farcs53$	...	...	...	...
b_3	...	...	$0\farcs0028$	...	$0\farcs007 \pm 0\farcs001$
x_3	...	...	$-0\farcs91$	...	$-0\farcs97$
y_3	...	...	$-1\farcs56$	...	$-1\farcs39$
Mid-IR Flux Ratios					
A2/A1	1.0018	1.0058	0.9218	1.0320	0.9227
B/A1	0.3318	0.3415	0.3438	0.3308	0.3354
C/A1	0.1690	0.1712	0.1691	0.1614	0.1680

Note. — The best-fit parameters for our two– and three–galaxy models based on the mid-IR data alone (left three columns) and after adding the VLBI constraints (right two columns). In the first column, G2 is modeled as a pseudo-Jaffe potential with scale length a_2'. In the remaining columns, G2 is modeled as an SIS. The subscripts differentiate between the main lens (1), secondary lens galaxy G2/object "X" (2), and a third lens mass (3). The χ^2 is broken down into the contributions from the image positions (χ^2_{pos}), flux ratios (χ^2_{flux}), lens position (χ^2_{gal}), and the priors on e and γ (χ^2_{prior}).

$z_l = 0.96$ for G1 (Tonry & Kochanek 1999), we estimate a best-fit mass of $\sim 3 \times 10^6\ M_\odot$ and $\sim 10^{10}\ M_\odot$ enclosed within the Einstein radii of G3 and G2, respectively, based on the mid-IR constraints alone, as compared to $\sim 5 \times 10^{11}\ M_\odot$ for G1. The statistical significance of finding $\Delta\chi^2 = 25$ for 3 additional parameters is 0.28 (a 72% confidence level) based on the F-test. When G2 is modeled as a pseudo-Jaffe potential, we find similar results for a three–galaxy model but with $\chi^2/\mathrm{dof} = 5.8$ (and an F-test confidence level of 45%). We conclude that G2 is better modeled as an SIS than a pseudo-Jaffe potential and therefore do not list the model parameters for a three–galaxy (SIE+pJaffe+SIS) model here.

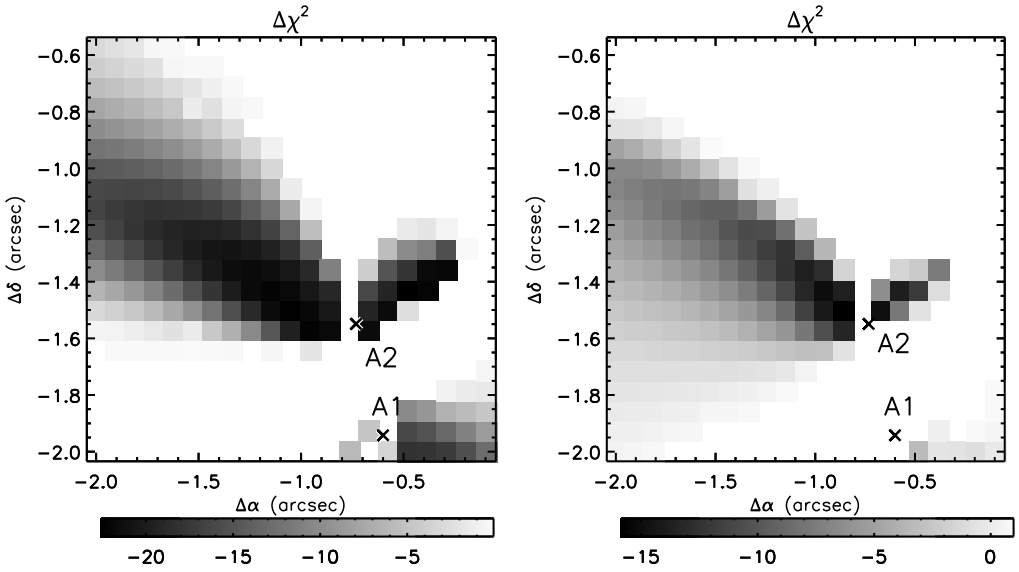

Fig. 3.— $\Delta\chi^2$ improvement resulting from adding a third lens galaxy to MG0414+0534 as a function of its position. In the left panel, only the mid-IR constraints are used in the models. In the right panel, only the radio constraints are used. The white regions are where the χ^2 either matched or exceeded the best value from the 2-galaxy models. North is up, East is left.

3.1. Radio Constraints: 8.4 GHz VLBI Structures

Fortunately, we can further test this model by adding the flux ratios and positions of the components detected in the radio with VLBI (Ros et al. 2000; Trotter et al. 2000), where each quasar image is resolved into core and jet structures. We added the core components a and b detected in the VLBI maps, and the VLBI jet structures c and d. The radio positions were constrained using the error ellipses shown in Figure 4. Note that Trotter et al. (2000) constrained their models using tighter constraints on the component positions while ours are more conservative, especially along the jet structures, to allow more freedom in the component cross-identifications. We find a better agreement ($\Delta\chi^2 = 3$) between the optical and radio core positions when shifting the HST images counter-clockwise by 0.1°, which is well within the HST astrometric uncertainties. For the remaining models, we assume the rotated HST positions for the mid-IR images (gray circles) and lens galaxies. Our best-fit component positions are indicated with symbols.

We list the best-fit model parameters for a two–galaxy model in Table 3. Here, we adopt an SIS profile for G2 since it provides a marginally better fit in this case than a pseudo-Jaffe profile. Our two–galaxy model has dof = 41, since there are four additional sources, each with three flux ratios and four pairs of (x, y) image coordinates as constraints, and four additional source positions as free parameters.

Figure 5 shows the resulting χ^2 improvement when adding a third lens galaxy in the same fashion as before, but including the constraints from all four radio sources (a similar map using the radio constraints only is shown in the right panel of Figure 3). The best-fit mass scale b_3 is also shown. The overall results are consistent with those based only on the mid-IR data, but with a narrower region extending to the Northeast (145° North of West) for the position of the third galaxy. The parameters for the best three–galaxy model with $(x_3, y_3) = (-0\farcs97, -1\farcs39)$ and $\chi^2/\mathrm{dof} = 1.6$ are listed in Table 3. If we vary the mass

parameter of G3, we find it is well-constrained to $b_3 = 0\farcs007 \pm 0\farcs001$ despite the freedom to simultaneously adjust all other model parameters, including the external shear. This corresponds to $10^{7.3\pm0.2}\ M_\odot$ enclosed within the Einstein radius at $z_l = 0.96$. The statistical significance of this result is $> 99\%$ based on the F-test.

The critical and caustic curves for our final three–galaxy model are shown in Figure 6. The third galaxy distorts the critical curves near images A1 and A2, bringing their flux ratio back into agreement with the mid-IR data. G3 may be associated with a faint dwarf galaxy or a nonluminous darkmatter substructure, as there are no nearby objects detected in the H-band image which are coincident with its predicted positions. Unfortunately, in the H-band image where we would best be able to detect G3, the estimated position lies almost exactly on the first Airy ring of image A2 (where the image subtraction residuals are high) and in a region with substantial emission from the quasar host galaxy, making it impossible to place useful limits on the mass-to-light ratio of G3.

The orientation of the external shear in our three–galaxy model, indicated in Figure 6, is in the same general direction as another object (G6) found $4\farcs4$ Southwest of image C in the H-band image. As pointed out by Falco et al. (1997), G6 is a possible compact group of galaxies, as it consists of three visible galaxies within 1" of each other. If we assume that G6 and G2 are at the same redshift as G1 and scale the Einstein radii of these objects by their I-band fluxes assuming a standard Faber-Jackson relation ($L \propto \sigma^4$), we can estimate the deflection scale of G6 as $b_6 = b_{G2}(L_6/L_{G2})^{1/2}$, using the fact that $b \propto \sigma^2$ for an SIS. Adopting the I-band magnitudes of G2 (24.769) and G6 (23.16) from Falco et al. (1997), we estimate $b_6 = 0\farcs34$. The shear caused by G6 is then $\gamma_6 = b_6/2r_6 = 0.03$, where r_6 is the angular separation from G1, and the amplitude of any higher order perturbations is $b_6 b_{G1}/r_6^2 = 0.013$ (see Kochanek et al. 2006). Since $\gamma_6 < 0.09$, G6 does not appear massive enough to fully explain the external shear in our three–galaxy model, although it

likely contributes some shear. The inclusion of G6 as a fourth lens mass yields a best-fit with $b_6 = 0\farcs21$, a reduction in shear amplitude (0.061), and a minor change in the shear orientation (53.3°) with $\chi^2/\mathrm{dof} = 52.6/37 = 1.4$.

In an attempt to bring our reduced χ^2 closer to unity, we tried adding a fifth lens galaxy on a grid of positions while optimizing the overall lens properties. We find the best improvement ($\Delta\chi^2 \approx 7$) near image C, extending to a region ∼2" North of G6. However, the reduced χ^2 does not improve ($46/34 = 1.4$). We conclude that additional substructures are unlikely to lead to a significant improvement of the fit given the constraints adopted here.

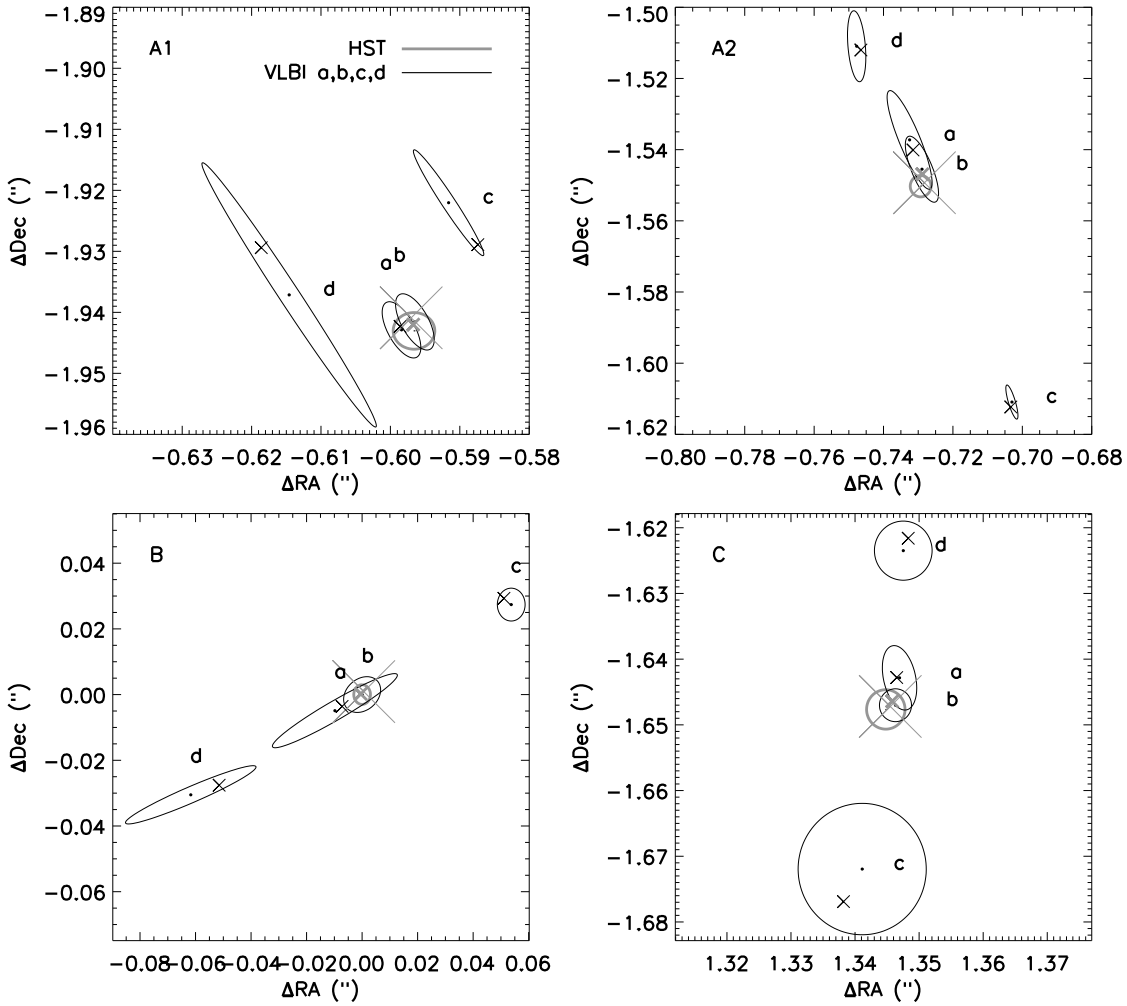

Fig. 4.— The constraints on the positions of the five sources used in our final model are shown in the image plane as error ellipses. Our estimates for the VLBI core components (a and b) and jet structures (c and d) from Ros et al. (2000) are shown as black ellipses. The error circles for the mid-IR positions are shown in gray. The best-fit positions for each component are indicated by the symbols and are consistent with each error ellipse. The larger symbols correspond to the mid-IR image positions, and the smaller, thick gray symbols correspond to VLBI component b.

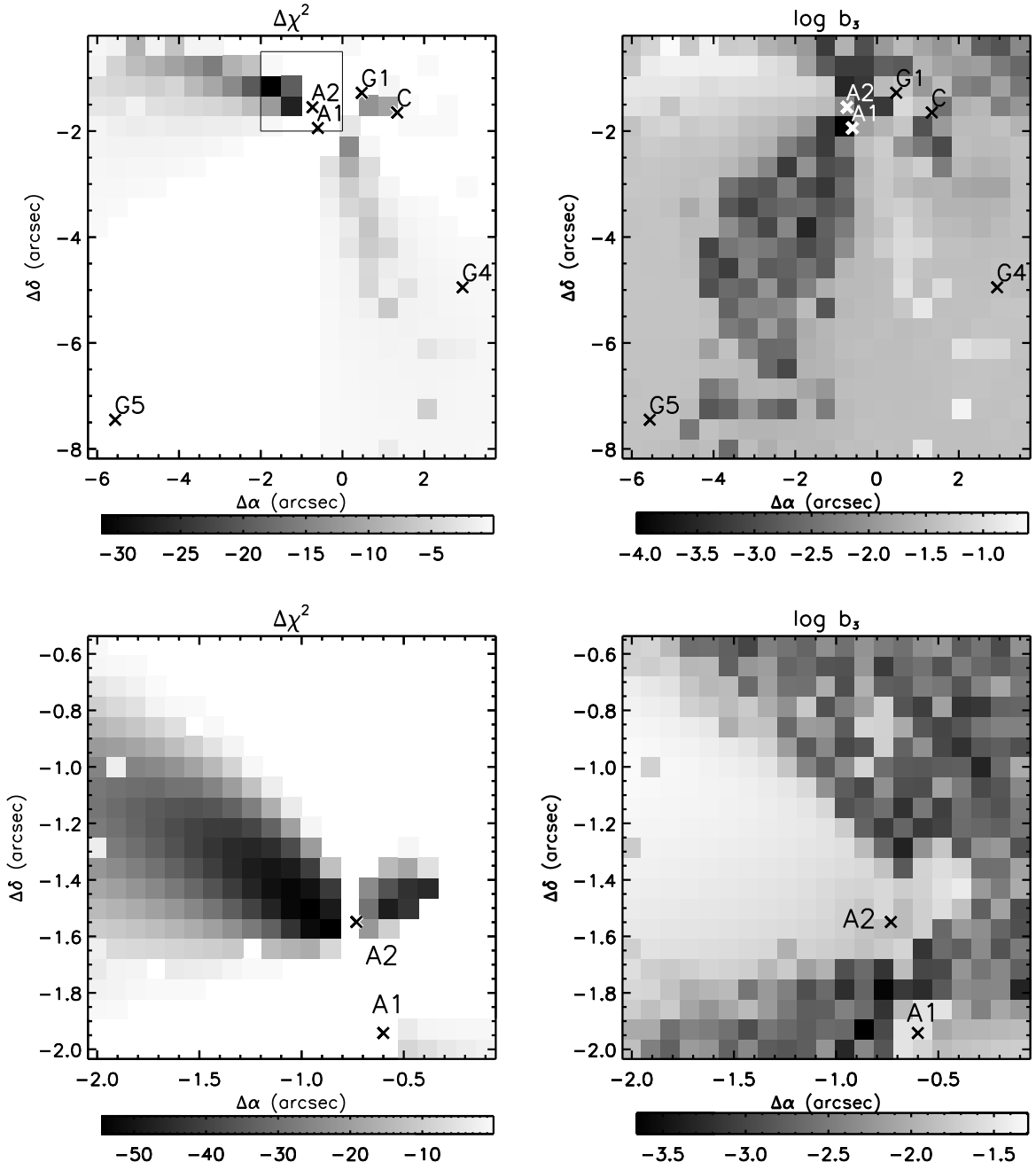

Fig. 5.— The left panels show the $\Delta\chi^2$ improvement resulting from adding a third lens galaxy as a function of its position, as in Fig. 3, but using both the mid-IR and radio constraints on the models. The right panels show the best-fit critical radius for the substructure. The bottom panels give an expanded view of the region indicated by the box in the top-left panel. The positions of two nearby galaxies G4 and G5 seen in the H-band image are also indicated.

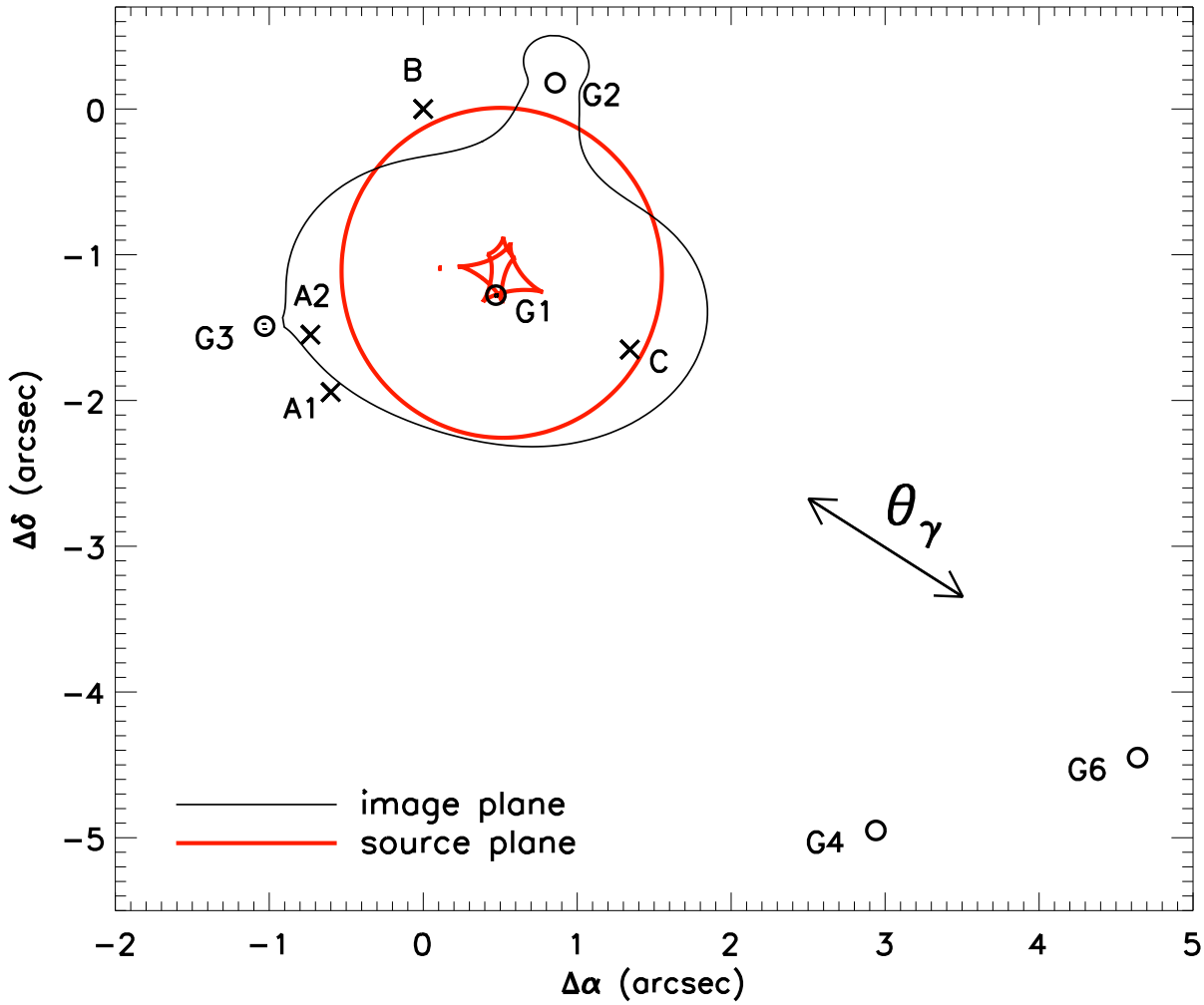

Fig. 6.— Best-fit critical (thin) and caustic (red) curves for our three–galaxy model when including both the mid-IR and radio constraints. Galaxy (image) positions are indicated with open circles (crosses). The direction of the external shear is indicated with arrows, and points toward another galaxy (G6) detected in the H-band image.

4. Discussion

Gravitationally lensed quasars are useful astrophysical tools because they allow us to study both the lens mass distribution and the background quasar. Unlike microlensing, where time variability can be used to isolate the effect, the effects of millilensing need to be disentangled from other physics that modify flux ratios. Mid-IR observations are ideal for this purpose because the effects of both microlensing and extinction are negligible. In MacLeod et al. (2009), we used the mid-IR flux ratios for the lens H1413+117 to show that flux ratio anomalies can detect companion lens galaxies, albeit a luminous companion in that system. This technique can also be used for detecting dark subhaloes in the lens, down to $10^5 M_\odot$ (Mao & Schneider 1998; Metcalf & Zhao 2002). As shown here and in Minezaki et al. (2009), the quadruply lensed quasar MG0414+0534 exhibits a flux ratio anomaly at mid-IR wavelengths that suggests there is millilensing substructure in the lens or along the line of sight to the quasar.

When we model either the mid-IR or radio data or both using only two lens galaxies (the primary lens G1 and a secondary lens G2/object X), we are unable to reproduce the observed flux ratios. When we add a third lens G3 near image A2, we obtain a significantly improved fit to the flux ratios. The optimal location of the substructure, roughly $0\farcs29$ to the Northeast of image A2 and $1\farcs45$ East of G1, was determined by adding a third lens on a grid of positions in the lens plane and varying its mass along with the overall lens properties. We are unable to associate the substructure with any source in the H-band image from *HST*, which suggests the third galaxy is either very faint or nonluminous. We derive a mass of $10^{7.3\pm0.2}$ $M_\odot$ enclosed within the Einstein radius at $z_l = 0.96$ for the substructure when modeled as an SIS, and our results are statistically significant at $> 99\%$ confidence based on the F test. Our findings are generally consistent with the less detailed models of Minezaki et al. (2009). The anomaly in the mid-IR suggests the presence

of a third lens galaxy which we assume is at the redshift of the main lens, although the structure could theoretically lie at some other redshift along the line of sight (Xu et al. 2012; Inoue & Takahashi 2012). There is also evidence for some contribution to the flux ratios from the neighboring galaxy group (G6) in the H-band image.

Besides being relevant to studying the background quasar, the search for subhaloes in the lens is also cosmologically important, because it offers the only means of identifying dark, low mass halos other than detection of γ-ray annihilation signals by Fermi. Sufficiently massive structures can be detected through their perturbations of image positions as seen with object X here, or in MG2016+112 (Kochanek 2006) and B1938+666 (Vegetti et al. 2012). Lower mass structures can only be detected through flux ratio anomalies, where the challenge is to obtain flux ratios unaffected by absorption or microlensing. The mid-IR satisfies these requirements but is limited at present by either poor resolution, as in Spitzer observations, or poor sensitivity, as in ground-based measurements. The LBTI mid-IR imaging interferometer (Hinz et al. 2003) on the Large Binocular Telescope (LBT) is a promising near-term solution, and a complete survey will be trivial with the advent of the James Webb Space Telescope.

This work is based on observations obtained at the Gemini Observatory (with Program ID GN-2005B-Q-43), which is operated by the Association of Universities for Research in Astronomy, Inc., under a cooperative agreement with the NSF on behalf of the Gemini partnership: the National Science Foundation (United States), the Science and Technology Facilities Council (United Kingdom), the National Research Council (Canada), CONICYT (Chile), the Australian Research Council (Australia), Ministrio da Cincia e Tecnologia (Brazil) and Ministerio de Ciencia, Tecnologa e Innovacin Productiva (Argentina). This work is based in part on observations made with the NASA/ESA Hubble Space Telescope. Support for program GO-7495 was provided by NASA through a grant from the Space

Telescope Science Institute, which is operated by AURA, Inc., under NASA contract NAS5-2655. EA is partially supported by National Science Foundation CAREER Grant No. 0645416. CSK is supported by NSF grant AST-1009756.

Facilities: Gemini (Michelle), HST (NICMOS).

REFERENCES

Agol, E., Gogarten, S. M., Gorjian, V., & Kimball, A. 2009, ApJ, 697, 1010

Bate, N. F., Floyd, D. J. E., Webster, R. L., & Wyithe, J. S. B. 2008, MNRAS, 391, 1955

—. 2011, ApJ, 731, 71

Belokurov, V., Zucker, D. B., Evans, N. W., et al. 2007, ApJ, 654, 897

Bullock, J. S., Kravtsov, A. V., & Weinberg, D. H. 2000, ApJ, 539, 517

Cohen, M., Walker, R. G., Carter, B., et al. 1999, AJ, 117, 1864

Congdon, A. B., & Keeton, C. R. 2005, MNRAS, 364, 1459

Dalal, N., & Kochanek, C. S. 2002, ApJ, 572, 25

Evans, N. W., & Witt, H. J. 2003, MNRAS, 345, 1351

Fadely, R., & Keeton, C. R. 2012, MNRAS, 419, 936

Falco, E. E., Lehar, J., & Shapiro, I. I. 1997, AJ, 113, 540

Hewitt, J. N., Turner, E. L., Lawrence, C. R., Schneider, D. P., & Brody, J. P. 1992, AJ, 104, 968

Hinz, P. M., Angel, J. R. P., McCarthy, Jr., D. W., Hoffman, W. F., & Peng, C. Y. 2003, in Society of Photo-Optical Instrumentation Engineers (SPIE) Conference Series, Vol. 4838, Society of Photo-Optical Instrumentation Engineers (SPIE) Conference Series, ed. W. A. Traub, 108–112

Inoue, K. T., & Takahashi, R. 2012, ArXiv e-prints

Keeton, C. R. 2001, ArXiv Astrophysics e-prints

Keeton, C. R., Gaudi, B. S., & Petters, A. O. 2005, ApJ, 635, 35

Keeton, C. R., & Moustakas, L. A. 2009, ApJ, 699, 1720

Klypin, A., Kravtsov, A. V., Valenzuela, O., & Prada, F. 1999, ApJ, 522, 82

Kochanek, C. S. 2006, in Saas-Fee Advanced Course 33: Gravitational Lensing: Strong, Weak and Micro, ed. G. Meylan, P. Jetzer, P. North, P. Schneider, C. S. Kochanek, & J. Wambsganss, 91–268

Kochanek, C. S., & Dalal, N. 2004, ApJ, 610, 69

Kochanek, C. S., Morgan, N. D., Falco, E. E., et al. 2006, ApJ, 640, 47

Koopmans, L. V. E., Bolton, A., Treu, T., et al. 2009, ApJ, 703, L51

Kratzer, R. M., Richards, G. T., Goldberg, D. M., et al. 2011, ApJ, 728, L18

Lawrence, C. R., Elston, R., Januzzi, B. T., & Turner, E. L. 1995, AJ, 110, 2570

MacLeod, C. L., Kochanek, C. S., & Agol, E. 2009, ApJ, 699, 1578

Mao, S., & Schneider, P. 1998, MNRAS, 295, 587

Metcalf, R. B., & Zhao, H. 2002, ApJ, 567, L5

Minezaki, T., Chiba, M., Kashikawa, N., Inoue, K. T., & Kataza, H. 2009, ApJ, 697, 610

Moore, B., Ghigna, S., Governato, F., et al. 1999, ApJ, 524, L19

Muñoz, J. A., Mediavilla, E., Kochanek, C. S., Falco, E. E., & Mosquera, A. M. 2011, ApJ, 742, 67

Pooley, D., Rappaport, S., Blackburne, J. A., Schechter, P. L., & Wambsganss, J. 2012, ApJ, 744, 111

Roche, P. F. 2004, Advances in Space Research, 34, 583

Ros, E., Guirado, J. C., Marcaide, J. M., et al. 2000, A&A, 362, 845

Schechter, P. L., & Moore, C. B. 1993, AJ, 105, 1

Strigari, L. E., Koushiappas, S. M., Bullock, J. S., et al. 2008, ApJ, 678, 614

Tonry, J. L., & Kochanek, C. S. 1999, AJ, 117, 2034

Trotter, C. S., Winn, J. N., & Hewitt, J. N. 2000, ApJ, 535, 671

Tseliakhovich, D., & Hirata, C. 2010, Phys. Rev. D, 82, 083520

Vegetti, S., Lagattuta, D. J., McKean, J. P., et al. 2012, Nature, 481, 341

Willman, B., Blanton, M. R., West, A. A., et al. 2005, AJ, 129, 2692

Xu, D. D., Mao, S., Cooper, A. P., et al. 2012, MNRAS, 421, 2553

Yoo, J., Kochanek, C. S., Falco, E. E., & McLeod, B. A. 2006a, ApJ, 642, 22

Yoo, J., Tinker, J. L., Weinberg, D. H., et al. 2006b, ApJ, 652, 26